Structural, optical and magnetic characteristics of iron doped zinc oxide thin films

A. Z. Mahmoud[a,b] , E. M. M. Ibrahim[c], Lamiaa Galal[b,d], E. R. Shaaban[e*], E. S. Yousef[f,g]

[a]*Physics Department, College of Sciences and Art At ArRass, Qassim University, ArRass 51921, Kingdom of Saudi Arabia*

[b]*Department of Physics, Faculty of Science, Assiut University, Assiut 71516, Egypt*

[c]*Physics Department, Faculty of Science, Sohag University, Sohag 82524, Egypt*

[d]*Physics Department, Faculty of Science, Northern Border University, Arar 91431, Saudi Arabia*

[e]*Physics Department, Faculty of Science, Al-Azhar University, Assiut, 71542, Egypt*

[f]*Research Center for Advanced Materials Science (RCAMS), King Khalid University, Abha 61413, P. O. Box 9004, Saudi Arabia*

[g]*Physics Dep., Faculty of Science, King Khalid University, P. O. Box 9004, Abha, Saudi Arabia*

$Zn_{1-x}Fe_xO$ films with x = 0, 5, 10, 15 and 20 at.% were prepared under high vacuum by the electron beam gun evaporation. The impact of Fe doping concentration on the films' structural, optical and magnetic characteristics has been taken into account. The patterns of XRD for all films at various Fe concentrations showed wurtzite-type structures. The results show that the size of nano-films reduces from 24 nm (0%) to 11 nm (0.20%) with elevating Fe content, which is owing to the difference between the ionic radii of Zn and Fe. Peaks associated with the elements to be seen were visible in the XPS spectra of undoped and 10% Fe-doped ZnO nanoparticles produced by the precipitation process: zinc (Zn), iron (Fe), and oxygen (O). The optical constants (n, k) of the $Zn_{1-x}Fe_xO$ films were obtained by the SE measurements by an ellipsometric model, allowing for the verification of the Fe^{3+} ions in Fe-doped ZnO. With the addition of Fe, the energy band gap decreased from 3.44 eV to 3.28 eV. M-H measurements revealed room-temperature ferromagnetism in Fe-doped ZnO thin film. As the Fe concentration rises, the magnetization increases until it reaches a concentration of 15%, at which point it starts to decrease. This decrease in magnetization was attributable to the spinel phase, which was seen in the XRD spectra. These findings imply that Fe-doped ZnO is a highly suggested material for the creation of spintronic and optoelectronic devices.

(Received December 13, 2022; Accepted May 1, 2023)

Keywords: $Zn_{1-x}Fe_xO$ films, XPS, AFM, Spectroscopic ellipsometry (SE), Magnetic characteristics

1. Introduction

Due to the fact that DMSs provide electron spin in addition to charge in electronic devices, their use has significantly increased during the past few years. At ambient temperature, the broad band gap of ZnO, an n-type semiconductor, is 3.37 eV. (RT). It is abundant in nature, inexpensive, and non-toxic to living things. The material's optical, physical, chemical, and electrical characteristics are also good [1]. They serve as an integral component in transparent electrodes, transducers, solar cells, and gas sensors [2]. ZnO attracts growing interest from researchers in the field of spintronic applications due to its several beneficial features by doping with suitable transition metals [3]. The cations of non-magnetic semiconductors are changed to transition metal (TM) ions or rare earth ions to create materials known as diluted magnetic semiconductors (DMS)

* Corresponding author: esam_ramadan2008@yahoo.com
https://doi.org/10.15251/JOR.2023.193.239

[4]. Due to its potential use in spintronic devices that take advantage of the spin and electronic charge of magnetic materials, the ferromagnetism found in strain gauges has drawn intense attention [2]. Additionally, tuning of optical and ferromagnetic characteristics can result from the doping of transition metals in wide-bandgap semiconductors [5-8]. A critical need for strain gauges for spintronic devices is intrinsic ferromagnetism with a high Curie temperature [9, 10]. In order to create TM metal-doped wide-bandgap semiconductors with room temperature ferromagnetism, labour is being put into it (RTFM). The second phase of magnetic collections or in spintronic applications necessitate a Curie temperature (higher than Curie temperature) and intrinsic ferromagnetism (FM), which generates transition metal-doped ZnO. Since RTFM-based applications as well as Mn, Fe, and Co doped ZnO have been found in numerous ZnO systems [11]. Results for ferromagnetism in transition metal-doped ZnO have been reported, however they are often contradictory. For example, Liu et al. [12] detected RTFM and believed it to be an inherent property of Fe-doped ZnO. Additionally, it has been found that transition metals have little impact on the magnetic of Mn- and Fe-doped ZnO films [13]. By correctly changing the stoichiometry ratio of the Fe dopant, we can reduce the energy gap of the ZnO semiconductor material and produce a new material with properties that differ from their complementary counterpart. Interest in nano-sized Fe doped ZnO nanoparticles has increased significantly in this field. Wei et al. also discovered ferromagnetism in Fe-doped ZnO and associated to the second phase at high doping concentration [14] when they created Fe-doped ZnO nanostructures using chemical roots and attributed their formation to zinc vacancies (Zni) [15]. Despite multiple findings in the literature, there remains disagreement over the cause of the ferromagnetism seen in transition metal-doped ZnO strain gauges at ambient temperature. According to some hypotheses, adding these TMs will significantly alter the luminous and magnetic properties of ZnO nanoparticles. However, the mechanism underlying room temperature ferromagnetism (RTFM) in Fe doped ZnO is still not fully understood, and the relationship between magnetic and optical properties is not entirely evident as a result of conflicting findings in the literature. These incongruent results suggest that RTFM in (DMS) may be particularly sensitive to preparation methods. In order to explore the micro-structural characteristics, morphology, optical (through spectroscopic ellipsometry) and magnetic properties, this article will produce high-quality nano films of $Zn_{1-x}Fe_xO$ (x= 0, 0.05, 0.10, 0.15 and 0.20). Using the change in nano-structural parameters to explain the change in optical and magnetic characteristics of the films.

2. Experimental details

To produce $Zn_{1-x}Fe_xO$ powders with the necessary doping percentage (x = 0, 0.05, 0.10, 0.15, and 0.20), dissolve Zn (NO3)2.6H2O and an appropriate amount of Fe (NO3)2.6H2O (Sigma-Aldrich Co., USA) in 50 mL of distil water. Deionized water was used to dissolve the zinc and ferric nitrates, and the resulting solution was agitated for an additional hour. Drop by drop, NH4OH solution was added to the prepared solution until the pH reached 9. The mixture was agitated for three hours at room temperature before filtering. The precipitate was dried at 100°C for five hours. The powdered dry precipitates were used as beginnings for creating films. $Zn_{1-x}Fe_xO$ thin films (x = 0, 0.05, 0.10, 0.15, and 0.20) were deposited in an Edward 306Auto deposition equipment using an electron beam gun during high vacuum (see Figure I). Clean the Corning #1022 glass substrate that has been placed with care. Fill the graphite boat with mass $Zn_{1-x}Fe_xO$ before beginning the evaporation process and set the vacuum system to a pressure of around 9 10-7 mbar. In order to increase film adhesion, the substrate temperature was held at 150 °C, and the deposition was entirely controlled by an evaporation rate of 2 nm/min. Zn1xFexO films were evaluated for phase pass using a Philips X-ray diffractometer (model X'pert) using Cu-$K_{\alpha 1}$ radiation (λ = 1.54 Å). The XRD data were collected in step-scan mode at the diffraction angles. Pure silicon was used to calibrate the device (99.9999). The fundamental makeup of the films was examined using an energy dispersive X-ray spectrometer (EDXS) and a SEM (JOEL XL) running at 30 kV power. To assess the band structure's property, spectroscopy and (XPS) photoelectron spectroscopy were used. Using spectroscopic ellipsometry data (ψ, Δ) and a three-layer model system, optical constants are extracted. We used a vibrating sample magnetometer

(VSM-9600M-1, USA) to conduct field-dependent magnetization (M-H) experiments in magnetic fields up to room temperature to investigate the magnetism of $Zn_{1-x}Fe_xO$ (x = 0, 0.05, 0.10, 0.15, and 0.20).

3. Results and discussion

3.1. Elemental composition analysis

Chemical Compositions analysis of undoped ZnO and Fe doped ZnO nanoparticles were investigated by (EDXS). Fig. 1. displayed the EDXS spectra for pure ZnO and $Zn_{0.90}Fe_{0.10}O$ nano-films which indicates that all the samples are consists of Zn, O or Fe, confirming that the incorporated of Fe into the samples. The EDXS analysis revealed that the nano-films with our selected ratios are nearly stoichiometric.

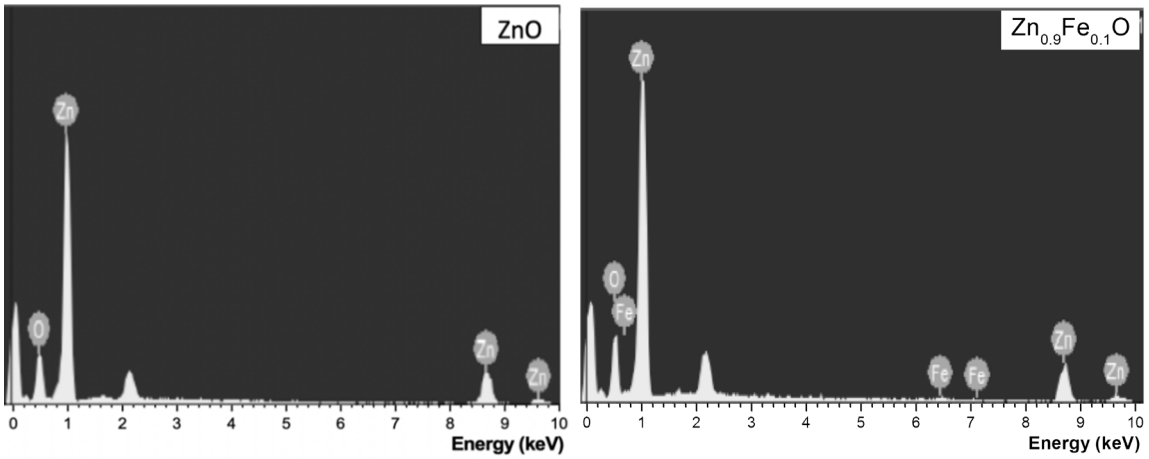

(a) *(b)*

Fig. 1. Energy-dispersive analysis X-ray (EDAX) spectrum of (a) ZnO, (b) $Zn_{0.9}Fe_{0.1}O$ thin films.

3.2. Microstructural characterization

Figure 2 (a) describes the X-ray diffraction of the $Zn_{1-x}Fe_xO$ (x= 0, 0.05, 0.10, 0.15, and 0.20) films. According to the cryptography code # 00-900-4178, all films of $Zn_{1-x}Fe_xO$ have a single hexagonal ZnO phase and space group P63mc. It was noted that no contamination, such as Fe cluster, FeO, Fe3O4, or Fe2O3, was found at the Fe doping concentrations of 5 at.% to 15 at.%, indicating that the amount of iron is less than the solubility limits. However, we cannot completely rule out the potential of secondary amorphous phase improvement clusters or precipitates that are too small to be picked up by XRD observations. Due to the difference in ionic radii between Fe and Zn, the incorporation of dopant ions into the basic cell of the powders results in the exitance of the tensile strain in the host (Zn). To further explain, Fe^{2+} and Fe^{3+}, two stable forms of Fe, have ionic radii of 0.78 Å and 0.68 Å, respectively. Zn^{2+} ionic radius is 0.74 Å, nevertheless. Due to the difference in ionic radius between Fe and Zn ions, when Zn^{2+} is substituted by Fe^{2+} or Fe^{3+} ions, the lattice of ZnO is deformed. Because Fe^{3+} has a smaller ionic radius (0.68 Å) than Zn2+ (0.74 Å) in this study, the film has undergone tensile strain. Because of the strain in the ZnO lattice, the distance between the planes gets shorter, which causes the peaks to move toward higher 2values as shown in Fig. 2. (b). However, a different phase known as spinel was formed when the concentration of Fe increased by more than 15%. The amount of iron that was not totally soluble during the formation of this phase may also be referred to. Since the intensity is proportional to the atomic number of the components, the XRD peaks' intensity continuously decreases as the Fe concentration rises (Z). As a result, the intensity of the peaks decreases when Zn (Z=30) is substituted by Fe (Z=26), which has a lower Z value.

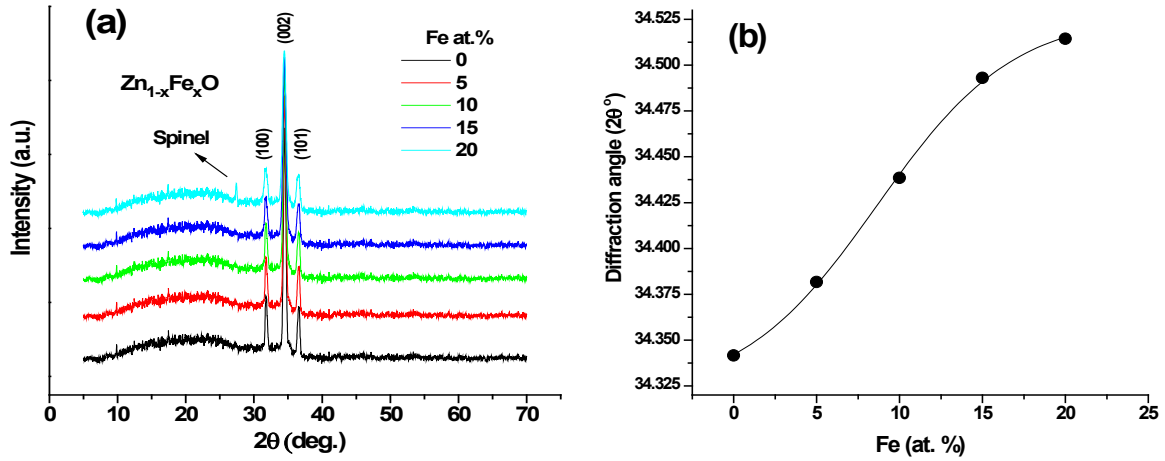

Fig. 2. (a) XRD patterns of $Zn_{1-x}Fe_xO$ thin films (b) diffraction angle versus Fe content.

Then, the lattice constants (a, c) have been computed. The obtained lattice parameters are plotted in Fig. 3. The lattice parameters 'a' and 'c' of the wurtzite structure of Fe-doped ZnO and ZnO films can be recorded utilizing the plane spacing equation [16, 17]:

$$\frac{1}{d_{hk\ell}^2} = \frac{4}{3}\left(\frac{h^2+hk+k^2}{a^2}\right) + \frac{\ell^2}{c^2} \tag{1}$$

where a & c are the lattice parameters, d is the interplanar distance and (hkl) are the Miller indices with the first-order approximation (n = 1) for the (100) plane and using the Bragg equation $n\lambda = 2d_{hk\ell}sin\theta$ The lattice parameter 'a' and 'c' is obtained from the relations

$$a = \frac{\lambda}{(\sqrt{3}\sin\theta_{100})} \quad \& \quad c = \frac{\lambda}{\sin\theta_{002}} \tag{2}$$

The lattice parameters "a" and "c" have values that are in great agreement with the typical values for ZnO single crystals (a = 3.250 Å and c = 5.207 Å), demonstrating the exceptional quality of the ZnO thin films. The values "a" and "c" of the lattice parameters are smaller in the compressed films than in the bulk doped films [18]. As the iron content increases, the lattice parameters "a" and "c" in $Zn_{1-x}Fe_xO$ films decrease, as shown in Fig. 3. The ZnO and Fe doped ZnO wurtzite structures have almost perfect shape, as seen by the lattice parameter's c/a ratio.

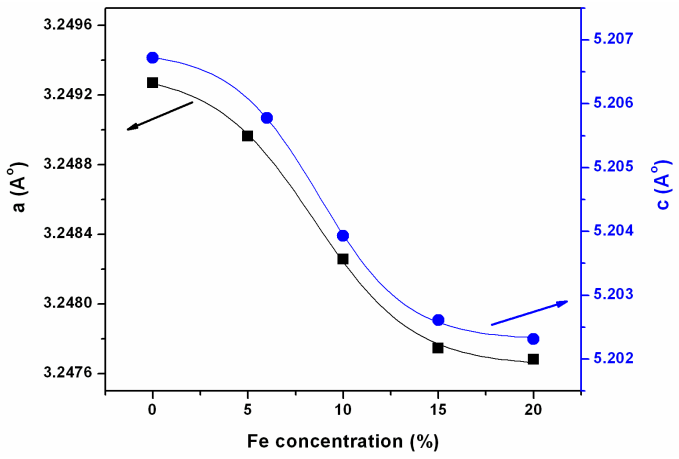

Fig. 3. Lattice parameters "a" and "c" against Fe concentration for $Zn_{1-x}Fe_xO$ thin films.

It is feasible to eliminate the instrumental broadening input by obtaining a diffraction pattern from the line broadening of a typical material and applying the following Eq. [19]:

$$\beta_{hkl}(2\theta) = \sqrt{(\beta_{hkl})^2_{measured} - (\beta_{hkl})^2_{standard}} \quad (3)$$

Here β_{hkl} is the (FWHM) collected of crystallite-size broadening, β_c and lattice-strain broadening, β_s:

$$\beta_{hkl} = \beta_c + \beta_s = \frac{k\lambda}{D\ cos\theta_o} + 4\varepsilon(sin\theta_o) \quad (4)$$

where k is shape factor (≈ 0.9), D is crystallite size, and λ is wavelength of the CuK_α radiation and ε is the lattice strain.

The films' crystallite size was recorded by utilizing the well-known Debye –Scherrer's formula [19, 20]

$$D_v = \frac{k\lambda}{\beta_{hkl}\cos(\theta)} \quad (5)$$

where λ is the wavelength (1.54 Å)

The lattice strain (ε) parameter is calculated using the following relation [19, 20]

$$\varepsilon = \frac{\beta}{4tan\theta} \quad (6)$$

Fig. 4 shows the values of the microstructural parameters D_v and ε for $Zn_{1-x}Fe_xO$ films with varied Fe concentrations. It is obvious that the crystallite size decreases with increasing Fe content, going from 24 nm (x=0) to 11 nm (x=0.20), while the lattice strain increases. It was discovered that only the preparation circumstances and structural disorder had a significant impact on the fluctuation in crystallite size [21]. The examined samples were prepared under nearly consistent preparation conditions, hence the decrease in crystal size is due to the substitution of Zn ions for Fe ions.

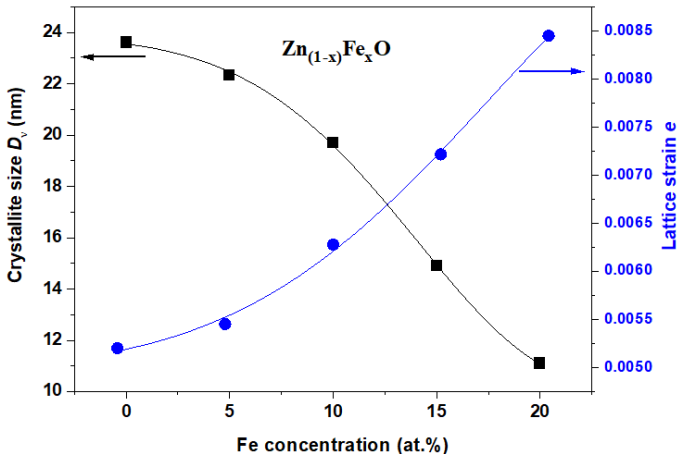

Fig. 4. Crystallite size and lattice strain $Zn_{1-x}Fe_xO$ films as a function of Fe content.

3.3. X-Ray photoelectron spectroscopy (XPS) studies

XPS is used to evaluate the chemical makeup of the elements present in equipped samples. All prepared films underwent an overview analysis. Overview spectra of undoped and 10% Fe-doped ZnO nanoparticles produced using the electron beam cannon approach are shown in Fig. 5 (a and b) at energies between 0 and 1200 eV. These data show maxima for the elements zinc (Zn),

iron (Fe), and oxygen (O). The O 1s area's asymmetric XPS spectrum shows the presence of multiple oxygen species. Multiple oxygen coordinates in the specimens may be to blame for the wide dispersion of the peaks. O ions occupying tetrahedral positions and being encircled by Zn atoms with wurtzite structures are attributed to the peak at the lower binding energy, which is 529 eV. The higher binding energy peak, which is approximately at 531 eV, is caused by the oxygen vacancy defect. It is evident that the satellite peaks and Fe 2p3/2 and Fe 2p1/2 peaks of the film have been identified. The 10% Fe-doped nano-films' Fe 2p3/2 and Fe 2p1/2 peaks, which have a peak spacing of 14 eV, can be observed in the figure to occur at 710 eV and 724 eV, respectively. The coupling of spin-orbit between the Fe atoms is the source of the variation in binding energy. The Zn 2p peak's binding energy was seen. The binding energies of the Zn 2p3/2 and 2p1/2 peaks for 10% Fe-doped ZnO are 1022 eV and 1045 eV, respectively. This proves that all films contain zinc in the Zn2+ state [22].

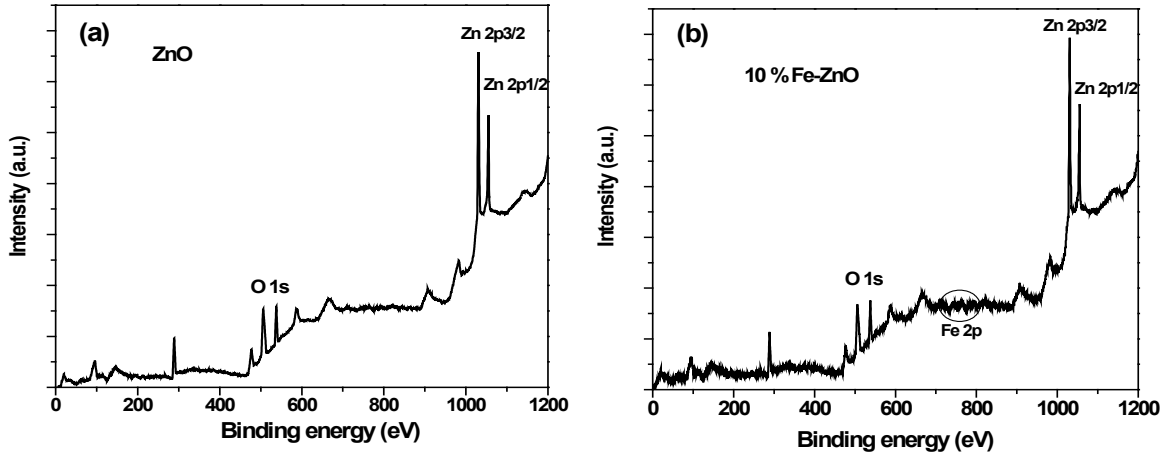

Fig. 5. XPS spectra for (a) pure ZnO and (b) $Zn_{0.90}Fe_{0.10}O$ films.

3.4. Spectroscopic ellipsometry and optical constants

By using spectroscopic ellipsometry SE, the refractive index, n, and absorption index, k, of the $Zn_{1-x}Fe_xO$ (0.0 x 0.2) films have been determined.

In these films, the SE obtaining parameters ψ and Δ are associated to the microstructure and optical properties through the following relation [22, 23]:

$$\rho = \frac{r_p}{r_s} = \tan\psi \exp(i\,\Delta) \tag{6}$$

where r_s and r_p are the Fresnel's coefficients of reflection for the films.

Fig. 6 (a, b) are the SE, ψ and Δ developed at an incident angle 70° on $Zn_{1-x}Fe_xO$ films.

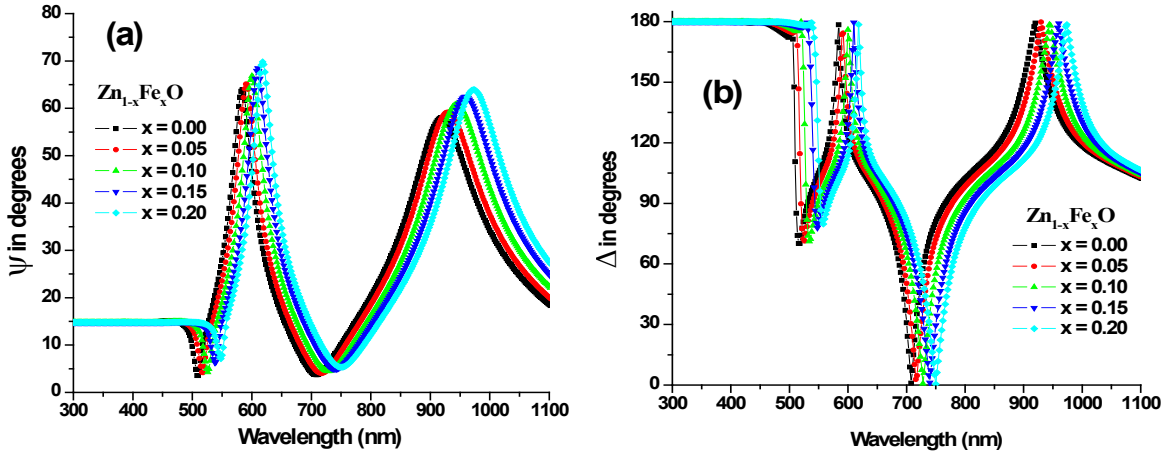

Fig. 6. The experimental ellipsometry data for parameters (a) Psi (ψ) and (b) Delta (Δ) for $Zn_{1-x}Fe_xO$ thin films

A three-layer optical model was used to determine *n*, *k* and film thickness d: upper (rough) layer/ "B-spline" absorbing $Zn_{1-x}Fe_xO$ layer/ substrate. The B-spline layer is partially transparent in this slide. Using least squares regression and a root mean square (RMS) function (σ), spectral changes in *ψ* and *Δ* were closely fitted [24]:

$$\sigma=\frac{1}{2\text{N-M}}\sum_{i=1}^{N}\left(\left(\frac{\psi_i^{\text{mod}}-\psi_i^{\text{exp}}}{\sigma_{\psi,i}^{\text{exp}}}\right)^2+\left(\frac{\Delta_i^{\text{mod}}-\Delta_i^{\text{exp}}}{\sigma_{\Delta,i}^{\text{exp}}}\right)^2\right) \tag{7}$$

A better fit with the acquired (experimental) data (symbols) over the whole spectrum range is illustrated by the simulated spectral dependence of and for $Zn_{1-x}Fe_xO$ films in Fig. 7 (a, b). All films' thicknesses have been calculated to be 160 2.72 nm, and roughness layer is 6.18± 0.13 nm, ref. [25] provides additional information on SE performance and its conceptual optical B-spline model.

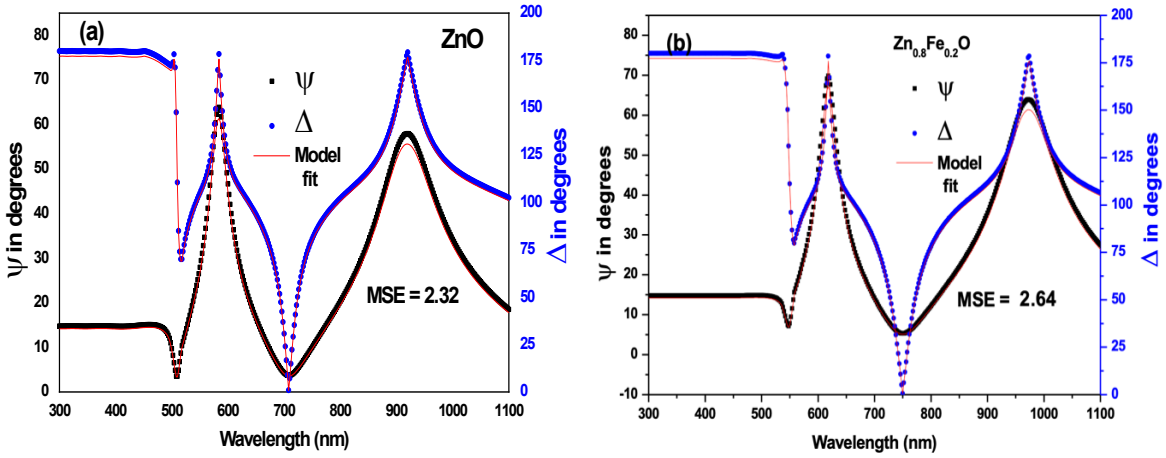

Fig. 7. The ellipsometric measured data (black and blue symbols) and the model fit (red line) for parameters Psi (ψ) and Delta (Δ) for (a)ZnO and (b) $Zn_{0.8}Fe_{0.2}O$ thin-films deposited in glass substrate.

The calculated values of the $Zn_{1-x}Fe_xO$ (x = 0, 5, 10, 15 and 20 at.%) films' refractive index, *n*, and extinction coefficient, *k*, are shown in Figs. 8(a, b), respectively. According to Fig.

8(a, b), the *n* and *k* steadily rise as the Fe concentration rises. All films in Fig (a, b) show a peak at around 380 nm, and *n* and *k* begin to decline at that wavelength, indicating an interband transition. In the visible spectral band, the extinction coefficient has a very low value.

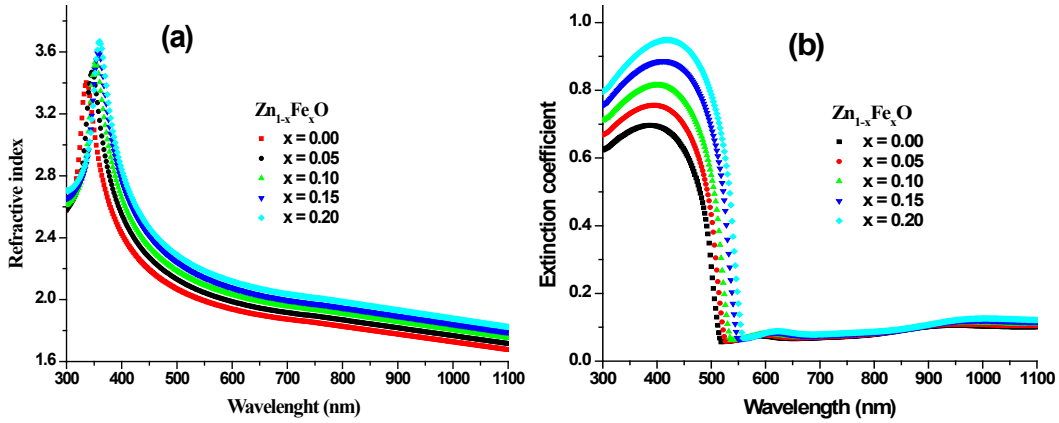

Fig. 8 (a) The refractive index and (b) extinction coefficient of $Zn_{1-x}Fe_xO$ thin films obtained by the SE method.

The absorption coefficient α of the $Zn_{1-x}Fe_xO$ films is correlated with absorption index, k by the relation ($k = \alpha\lambda/4\pi$). Fig. 9 (a) displays the plot of the absorption coefficient, α versus photon energy, *E* in eV.

The next Tauc equation [26, 27] provides the optical transitions of the analysed films in the strong absorption range ($\alpha \geq 10^4$):

$$\alpha(h\upsilon) = \frac{K'(h\upsilon - E_g^{opt})^x}{h\upsilon}$$

where E_g^{opt} is the energy gap and x is the suffix controlled by the type of transition that controls the optical absorption. As demonstrated in Fig. 9 (b), we plotted $(\alpha . h\nu)^x$ vs. $(h\nu)$ for $Zn_{1-x}Fe_xO$ films with different Fe contents and obtained the best fit at x = 2, thus a direct transition was approved. Estimated E_g^{opt} as the crossing of the extrapolation of the linear fit part with the photon energy axis.

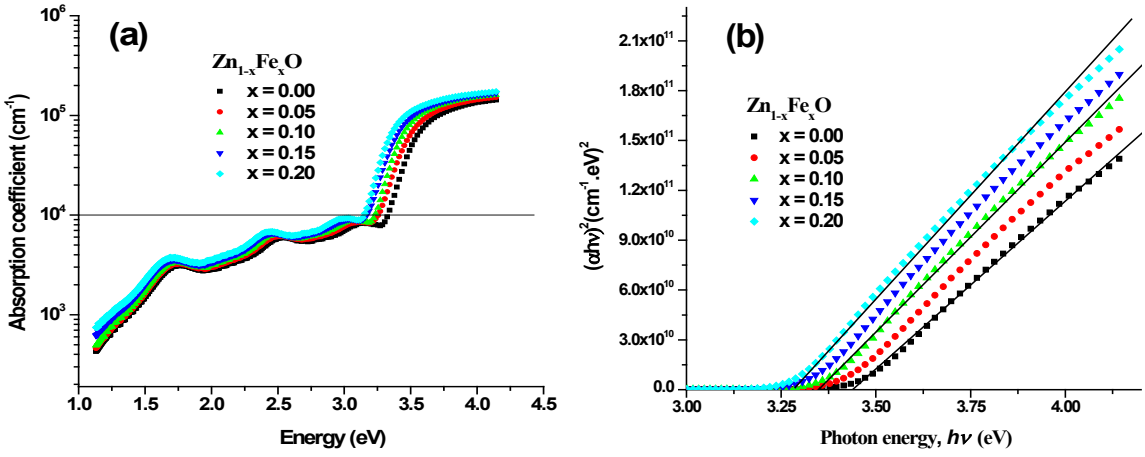

Fig. 9. (a) Absorption coefficient and (b) $(\alpha h\upsilon)^2$ versus hυ of $Zn_{1-x}FexO$ thin films obtained by SE method.

The findings demonstrate that, as shown in Fig. 10 (b), the E_g^{opt} values obtained decrease as the concentration of Fe increases. As Fe content rises, Zn atoms are gradually replaced by Fe, causing the fundamental band gap to shift to the red. More interstitial oxygen atoms are incorporated as impurities into the ZnO film as the Fe doping concentration rises, leading to more delocalized states and a narrower band gap. Additionally, the loss in crystallinity caused by the smaller crystals and greater microstrain, which result in less crystal development and more defects in the $Zn_{1-x}FexO$ films, can be responsible for the drop in band gap value.

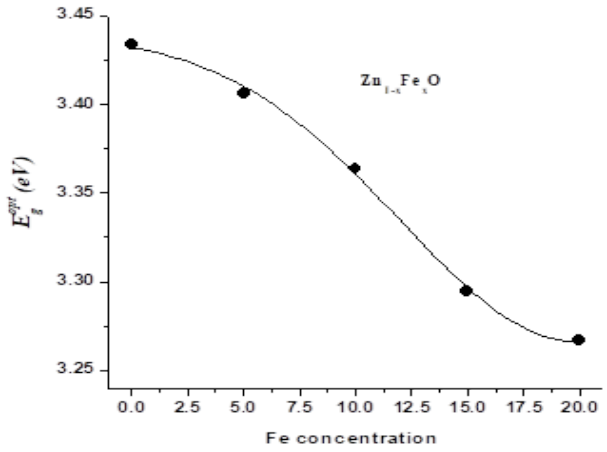

Fig. 10. Optica energy gap as a function of Fe concentration for $Zn_{1-x}FexO$ thin films.

3.5. AFM analysis Fedoped ZnO films

One of the best imaging methods now being employed at the nanoscale, sub-nanoscale level, and the surface topography is atomic force microscopy (AFM). AFM measurements can be used to quantitatively analyse the surface topographies of a film, including the grain size and surface roughness. Fig. 11 (a-e) illustrate the 3D AFM pictures of ZnO films with various Fe concentrations. According to Fig., the undoped film features fine, spherically formed grains that are evenly spread. 11 (a). According to AFM tests, grain size dropped and surface roughness rose as iron content rose. The nucleation and mobility of atoms on the surface are reduced as the proportion of Fe is increased. Fe doping in ZnO film has a reasonable impact on grain size and surface roughness, according to the AFM investigation.

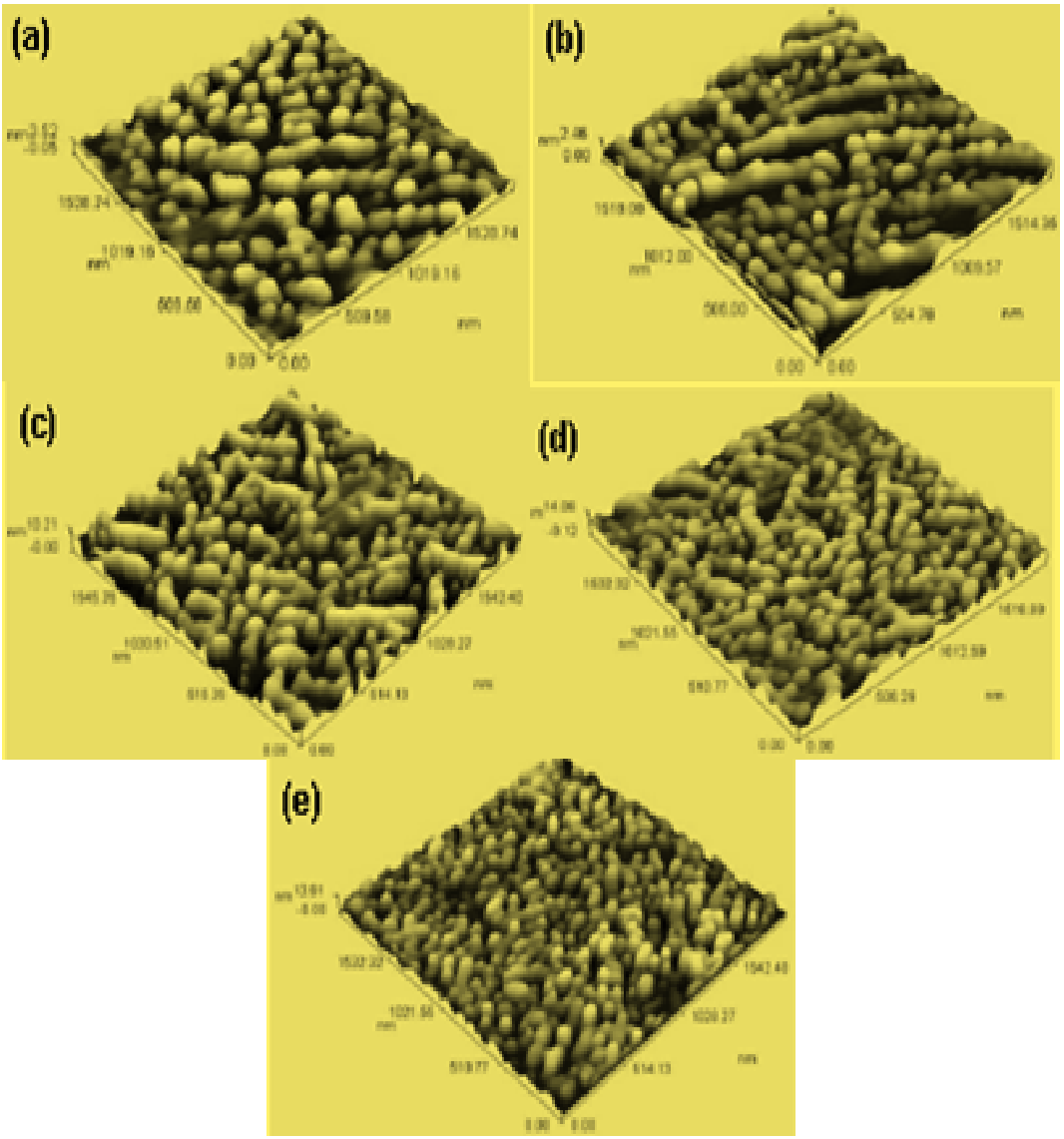

Fig. 11. AFM Images of Fe: ZnO films with (a) 0%, (b) 5%, (c) 10 %, (d) 15% and (e) 20 % Fe concentration.

3.6. Magnetic characterization

To better understand the magnetic behaviour of these Fe-doped ZnO nano-films with different concentrations (0, 5, 10, 15 and 20%), magnetization against field-dependent curves were measured at 300 K. Pure ZnO displays diamagnetic performance in Fig. 12, while Fe/ZnO nano-films demonstrate magnetization and RTFM increases with increasing Fe content. There was no indication of saturation in every of the considered specimens. The origin of the RTFM in Fe-doped ZnO nano-films can be clarified based on the XRD and SEresults. These results indicate that Fe^{3+} ions occupy Zn^{2+} sites within the lattice of the wurtzite ZnO crystal structure.

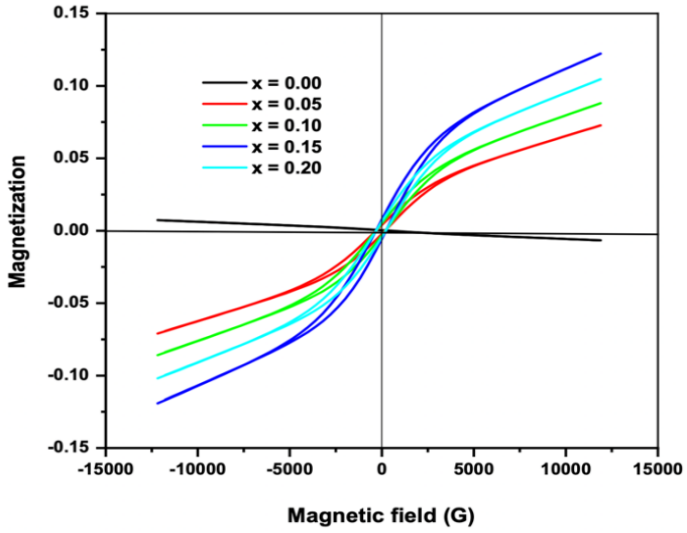

Fig. 12. Room temperature Magnetic hysteresis loops for $Zn_{1-x}Fe_xO$ ($0.0 \leq x \leq 0.20$) thin films.

It is evident from SE Spectroscopic Ellipsometry studies that Fe doping causes numerous Zn_i and Vo defects, which narrow the band gap. Therefore, it makes sense to conclude that adding Fe^{3+} in a ferromagnetic behavior may cause RTFM in materials with extensive Zn_i and Vo flaws. Ferromagnetism is therefore only produced via exchange interactions between local d-spins on Fe ions and free delocalized charge carriers originating from oxygen vacancies. It has been proposed that room temperature ferromagnetism depends critically on the interaction between defects and magnetism.

All Fe-doped ZnO nano-films' M-H plots can be seen to form hysteresis loops, indicating soft ferromagnetism in the room-temperature ferromagnetic behavior with a weak coercive field and low remanence. Iron-doped ZnO films have been reported by several groups to be ferromagnetic at and/or above room temperature [28, 29]. According to a theory put out [27, 28], the change in magnetization in Fe-doped ZnO is caused by the average distance between Fe ions shortening as Fe content increases. Therefore, the increased distance between Fe ions, which decreases the ferromagnetic interaction, can be used to explain the weak magnetization reported at low Fe levels in our work.

However, increasing the iron content strengthens the ferromagnetic interaction (shorter iron ion spacing), which raises the magnetization. With the exception of films with a high concentration of 20% Fe doping, the magnetic moment of the materials increases as Fe doping concentration rises. This is linked to the development of a binary phase, which lessens the concentration's magnetism. The spinel that was visible in the XRD spectra is in this phase. As seen in Fig. 12, this binary material is a ferrite called (Fe_2O_3) that blocks the magnetic field and lessens the substance's magnetism. 12.

4. Conclusions

$Zn_{1-x}Fe_xO$ films with x = 0, 5, 10, 15 and 20 at.% were prepared under high vacuum by the electron beam gun evaporation. The impact of Fe doping concentration on the films' structural, optical and magnetic characteristics has been taken into account. The patterns of XRD for all films at various Fe concentrations showed wurtzite-type structures. The results show that the size of nanoparticles reduces from 24 nm (0%) to 11 nm (0.20%) with elevating Fe content, which is owing to the difference between the ionic radii of Zn and Fe. Fe doping can be used to regulate how well ZnO nano-films absorb light and change their energy gap. Peaks associated with the elements to be seen were visible in the XPS spectra of undoped and 10% Fe-doped ZnO nanoparticles produced by the precipitation process: zinc (Zn), iron (Fe), and oxygen (O). The

optical constants (n, k) of the $Zn_{1-x}Fe_xO$ films were obtained by the SE measurements by an ellipsometric model. With the addition of Fe, the energy band gap decreased from 3.44 eV to 3.28 eV. This is because more interstitial oxygen atoms are incorporated into the ZnO film as impurities, leading to more delocalized states and a smaller band gap. As the Fe concentration rises, the magnetization increases until it reaches a concentration of 15%, at which point it starts to decrease. This decrease in magnetization was attributable to the spinel phase, which was seen in the XRD spectra. This binary substance, (Fe_2O_3), is a ferrite that obstructs the magnetic field and lessens the film's magnetism. These findings imply that Fe-doped ZnO is a highly suggested material for the creation of spintronic and optoelectronic devices.

Acknowledgments

This work was supported by the King Khalid University through a grant RCAMS/ KKU/03-22 under the Research Center for Advance Materials (RCAMS) at King Khalid University, Saudi Arabia.

References

[1] H.Y. Xu, X. L.Liu, D. L. Cui, M. Li Jiang and M. H, Sens. Actuators B. 114 (2006) p. 301; https://doi.org/10.1016/j.snb.2005.05.020

[2] B. Pal, S. Dhara, P.K. Giri and D. Sarkar, J. of Alloys and Compounds. 647 (2015) p. 558; https://doi.org/10.1016/j.jallcom.2015.05.218

[3] C. Aydın, M.S. Abd El-sadekb, Kaibo Zheng, I.S. Yahiad and F. Yakuphanoglu, Opt. & Laser Technol. 48 (2013) p. 447; https://doi.org/10.1016/j.optlastec.2012.11.004

[4] M.Emam-Ismail, M. El-Hagary, E.R.Shaaban, S. Althoyaib, Journal of Alloys and Compounds Volume 529, 2012, Pages 113-121; https://doi.org/10.1016/j.jallcom.2012.03.027

[5] A. Moezzi, A. M. McDonagh, and M. B. Cortie, Chemical Engineering Journal, vol. 185-186, pp. 1-22, 2012; https://doi.org/10.1016/j.cej.2012.01.076

[6] E.R.Shaaban, M.El-Hagary, M.Emam-Ismail, A.Matar, I.S.Yahia, Materials Science and Engineering: B 178, Issue 3, 2013, Pages 183-189; https://doi.org/10.1016/j.mseb.2012.11.005

[7] J. Zhang, S. Wang, M. Xu et al., Crystal Growth and Design, vol. 9, no. 8, pp. 3532-3537, 2009; https://doi.org/10.1021/cg900269a

[8] X. J. Liu, X. Y. Zhu, C. Song, F. Zeng, and F. Pan, Journal of PhysicsD: Applied Physics, vol. 42, no. 3, Article ID035004, 2009; https://doi.org/10.1088/0022-3727/42/3/035004

[9] J. R. Neal, A. J. Behan, R. M. Ibrahim et al., Physical Review Letters, vol. 96, no. 19, Article ID 197208, pp. 1-4, 2006' https://doi.org/10.1103/PhysRevLett.96.197208

[10] X. H. Huang, G. H. Li, B. Q. Cao, M. Wang, and C. Hao, Journal of Physical Chemistry C, vol. 113, no. 11, pp. 4381-4385, 2009; https://doi.org/10.1021/jp810790h

[11] Zhang ZH, Wang X, Xu JB, Muller S, Ronning C, Li Q (2009), Nat Nanotechnol 4(8):523; https://doi.org/10.1038/nnano.2009.181

[12] Liu H, Yang J, Zhang Y, Wang Y, Wei M (2008), Mater Chem Phys 112(3):1021-1023; https://doi.org/10.1016/j.matchemphys.2008.07.004

[13] Hong NH, Sakai J, Brizé V (2007), J Phys Condens Matter 19(3):03621; https://doi.org/10.1088/0953-8984/19/3/036219

[14] Wei XX, Song C, Geng KW, Zeng F, He B, Pan F (2006), J Phys Condens Matter 18(31):7471; https://doi.org/10.1088/0953-8984/18/31/037

[15] Mishra AK, Das D (2010), Mater Sci Eng B 171(1-3):5-1; https://doi.org/10.1016/j.mseb.2010.03.045

[16] Gharieb A.Ali, M.Emam-Ismail, M.El-Hagary, E.R.Shaaban, S.H.Moustafa M.I.Amer

H.Shaban, Optical Materials 119, (2021), 111312; https://doi.org/10.1016/j.optmat.2021.111312

[17] Galca, A.C., Socol, G. and Cracium, V. (2012), Thin Solid Films, 520, 4722-4725; https://doi.org/10.1016/j.tsf.2011.10.194

[18] Kim, P.Y., Lee, J.Y., Lee, H.Y., Lee, S.J. and Cho, N.I. (2008), Journal of Korean Physical Society, 53, 207-211; https://doi.org/10.3938/jkps.53.207

[19] Shaaban ER, Kansal I, Mohamed S., Ferreira J MF., Physica B: Condensed Matter. 2009; 404(20):3571-3576; https://doi.org/10.1016/j.physb.2009.06.002

[20] M El-Hagary, E R Shaaban, S H Moustafa, G M A Gad, Solid State Sciences 91 (2019) 15-22; https://doi.org/10.1016/j.solidstatesciences.2019.03.005

[21] M Emam-Ismail, M El-Hagary, E R Shaaban, S Althoyaib, Journal of alloys and compounds 529 (2012) 113-121; https://doi.org/10.1016/j.jallcom.2012.03.027

[22] Shaaban ER., J Alloys Compd. 2013; 563:274-279; https://doi.org/10.1016/j.jallcom.2013.02.132

[23] El-Naim A, Solieman A., Shaaban E. R., Journal of Materials Science: Materials in Electronics 31 (4) (2020) 3613-3621; https://doi.org/10.1007/s10854-020-02916-8

[24] Alzaid M., Mohamed W. S, El-Hagary M., Shaaban E. R., Hadia N. M. A., Optical Materials 2021, 118, 111228; https://doi.org/10.1016/j.optmat.2021.111228

[25] M. Emam-Ismail, A. Ali Gharieb, S.H. Moustafa, M.M. Mahasen, E R Shaaban, M. El-Hagary, Journal of Physics and Chemistry of Solids 157, 110195, (2021); https://doi.org/10.1016/j.jpcs.2021.110195

[26] J. Tauc, Materials Research Bulletin. 3 (1968).37-46; https://doi.org/10.1016/0025-5408(68)90023-8

[27] Srinivasulu T, Saritha K, Reddy KT., Mod Electron Mater. 2017; 3: 76-85; https://doi.org/10.1016/j.moem.2017.07.001

[28] Abdel-Baset TA, Fang YW, Anis B, Duan CG, Abdel-Hafiez M, Nanoscale Res Lett 11(1) (2016) 115; https://doi.org/10.1186/s11671-016-1332-x

[29] Beltrán JJ, Barrero CA, Punnoose A, Phys Chem Chem Phys 17(23) (2015)15284-15296; https://doi.org/10.1039/C5CP01408E